Lawrence Berkeley National Laboratory

Title
Towards super-resolution interference microscopy metrology of x-ray variable-line-spacing diffraction gratings: recent developments

Authors
Rochester, Simon
English, Damon
Lacey, Ian
et al.

Towards super-resolution interference microscopy metrology of x-ray variable-line-spacing diffraction gratings: Recent developments

Simon Rochester[a,*], Damon English[b], Ian Lacey,[c] Keiko Munechika,[d] and Valeriy V. Yashchuk[c]

[a]Rochester Scientific, LLC, 2041 Tapscott Ave., El Cerrito, CA 94530, USA;
[b]Engineering Division, Lawrence Berkeley National Laboratory, Berkeley, CA 94720, USA;
[c]Advanced Light Source, Lawrence Berkeley National Laboratory, Berkeley, CA 94720, USA;
[d]HighRI Optics, Inc., 5401 Broadway Terr, St. 304, Oakland, CA 94618, USA;

ABSTRACT

We report on recent work towards improving interference microscopy metrology of variable-line-spacing (VLS) x-ray diffraction gratings through a combination of techniques: image reconstruction to correct for distortion and blurring, multi-image super-resolution data acquisition to increase resolution beyond the single-image limit, and image stitching to increase the measurement area. Here, we concentrate on precision characterization and correction for lens distortion (aka geometrical distortion) and provide precise measurements of the effective image pixel distribution. We present and analyze the results of geometrical distortion measurements performed with test samples, including traditional checkerboard test artifacts and binary pseudo-random array (BPRA) standards patterned with two-dimensional uniformly redundant arrays (URA). The URA BPRA standards are also useful for measurement of the instrument transfer function (ITF), a measure of the optical aberrations and limited lateral resolution of the instrument. We also outline other essential elements and the next steps of the project on development of so-called super-resolution interference microscopy, enabling more precise measurements of VLS groove density than previously possible. The global aim of this project is to integrate our metrology technique into the manufacture of high-resolution x-ray gratings.

Keywords: variable line spacing grating, VLS grating, geometrical distortion, instrument transfer function, binary pseudo-random, super-resolution, power spectral density, interferometric microscope.

1. INTRODUCTON

Due to their focusing properties, VLS gratings have become the main elements of many x-ray spectrometers and monochromators [1,2]. Spectrometers with VLS gratings can disperse the spectrum in a focal plane almost perpendicular to the diffracted beams and allow formation of stigmatic spectral images. Steady improvements to these instruments have tightened the requirements for the shape (groove distribution, profile, and phase coherence) of the gratings. This necessitates the development of high-performance metrology for their characterization.

To enable fabrication of these optics at reasonable cost, advanced surface metrology with both high accuracy and high measurement rate must be available to integrate into modern deterministic surface figuring/patterning processes. When the optic is fabricated and ready for installation, additional surface metrology techniques are used at the x-ray facilities to ensure that the quality of the optical surface is adequate to the specifications of the beamline optical system and end-station. Confidence in the beamline optical design and fabrication specifications critically depends on the availability of trustworthy before-fabrication models of the optics, based on metrology data obtained with existing optics. Under- and over-specifications are both undesirable, the former because of the risk of beamline performance degradation, the latter due to the unnecessary cost increase.

Unfortunately, the existing metrology tools and data acquisition and processing methods are insufficient to meet today's challenges. The available metrology instrumentation in use at the x-ray light-source facilities, as well as in optical fabrication industry, including traditional long trace profilometry, deflectometry, interferometry, and microscopy, have essentially reached the limits set by modern state-of-the-art optical and mechanical materials and components, as well as by the nature of the physical processes used for measurement (see, for example, Refs. [3-7] and references therein).

*simon@rochesterscientific.com; phone 1 510 206-6586; https://www.rochesterscientific.com/.

Here we describe work designed to improve interference-microscopy-based metrology of variable-line-spacing (VLS) x-ray diffraction gratings. The technique [7], first suggested and demonstrated at the Advance Light Source (ALS) X-Ray Optics Laboratory (XROL) [8], is based on optical microscope measurements of the power spectral distributions (PSDs) of grating surface sub-areas and estimation of the groove density values from the spatial frequency of the corresponding PSD peaks (see Sec. 2). Under support of the U.S. Department of Energy (DOE) Small Business Technology Transfer (STTR) Program, we are working to advance the technique with higher accuracy and dynamic range of groove density variations than is currently available and make it suitable for integration into VLS x-ray grating fabrication processes. These goals are achieved by leveraging instrument characterization and data processing methods and procedures under development: image reconstruction to correct for distortion and blurring by the interferometric microscope in use, multi-image super-resolution data acquisition to increase resolution beyond the single-image limit, and high accuracy image stitching to increase the measurement area.

In this first publication on the project, we mostly concentrate on precision characterization (calibration) and correction of the interferometric microscope measurements for lens distortion (*aka* optical or geometrical distortion) and test a procedure for high accuracy measurement of the effective image pixel distribution. We present and analyze the results of geometrical distortion calibration (Sec. 3), performed with different test samples, including traditional checkerboard test artifacts and the binary pseudo-random array (BPRA) standards patterned two-dimensional (2D) uniformly redundant arrays (URA) [9,10]. The error introduced to the groove density measurement due to the geometrical distortion is illustrated on an example of a 600 lines/mm uniform blaze grating (Sec. 4). We also discuss the next essential developments of the project (Sec. 5): the next step is to implement the reconstruction (deconvolution) of the measured surface topography of a VLS grating based on the experimentally determined and analytically modeled instrument transfer function ITF of the tool in use (see Sec. 3.3). This enables sub-resolution interferometric microscope measurements with VLS x-ray gratings. Multiple sub-resolution measurements taken under sub-pixel displacement by a nano-motion stage are used (after the ITF correction) to produce even higher resolution topography data, constituting so-called super-resolution metrology technique. This cohesive approach allows more precise measurements of VLS groove density than previously possible. The global aim of this project is to integrate our metrology technique into the manufacture of high-resolution x-ray gratings.

2. OPTICAL METROLOGY WITH X-RAY VLS GRATINGS AT THE ALS XROL

The level of groove-density measurement accuracy desired for characteristic applications of VLS x-ray gratings can be illustrated by a typical case outlined in Ref. [7], related to the current design of the ALS MAESTRO beamline [11]. In this case, the VLS grating is specified with the groove density varying along the longitudinal coordinate x ($x = 0$ at the grating center) according to the polynomial function

$$g(x) = g_0 + g_1 \cdot x + g_2 \cdot x^2, \tag{1}$$

where $g_0 = 600$ lines/mm is the groove frequency at the center of the grating determining the x-ray energy range of the grating application, $g_1 \approx 0.25$ lines/mm^2 is desired to minimize the defocusing effect, and $g_2 \simeq 4 \cdot 10^{-5}$ lines/mm^3 is chosen to minimize the next order (coma) aberration. It is shown in Ref. [7] that even at rather relaxed tolerances for the parameters in Eq. (1) of

$$\delta g_0 / g_0 < 0.2\% , \ \delta g_1 / g_1 < 0.5\%, \text{ and } \delta g_2 / g_2 < 20\%, \tag{2}$$

a high measurement accuracy of $\sigma \leq 0.08$ lines/mm (corresponding to an absolute accuracy of about 100 nm/mm) is required. This and even higher accuracy is available with dedicated metrology instrumentation such as, for example, the precision interferometrically controlled comparator at the German National Metrology Institute (PTB) developed for precise calibration of linear encoders and line scales [12]. However, this unique instrumentation is hardly available at any metrology laboratory at the x-ray facilities around the world. Instead, typical methods utilize more common optical metrology tools.

2.1 Long trace profiler LTP-II based metrology of x-ray VLS diffraction grating

For a long time, the preferred tool for grating characterization at synchrotron radiation facilities [4,5,13-15] has been surface-slope-measuring long trace profilers (LTPs), arranged in the Littrow configuration for one dimensional (1D) measurements of the diffraction angle variation. In many cases, LTP metrology is capable of measuring groove density

distributions with the required accuracy, but, due to low spatial resolution, fails to measure groove phase coherence, which determines the beamline spectral resolution achievable with the grating.

Moreover, when applied to VLS gratings with rapid variation of the groove density, the LTP-based technique has fundamental limitations in both local accuracy and angular dynamic range. First, the steep variation of the groove density leads to a large variation of the optical path within the diffracted LTP sample light beam, causing a strong interference effect in the beam intensity distribution recorded with the LTP detector. This makes it practically impossible to measure the local diffraction angle with the required accuracy. Second, for strong groove density variation, the overall variation of the diffraction angle can significantly surpass the angular dynamic range of the LTP (typically ~ 10 mrad).

For example, spurious effects due to intra light-beam diffraction and interference and the limited angular range of the XROL LTP-II [16] have made impossible accurate metrology of the VLS grating developed for the ALS AMBER beamline [17] with rapid variation of the groove density specified with the parameters:

$$g_0 = 1000.1 \text{ lines/mm}, \ g_1 = 0.95381 \text{ lines/mm}^2, \ g_2 = 0.004007 \text{ lines/mm}^3, \text{ and } g_3 = -3.304 \times 10^{-6} \text{ lines/mm}^4. \quad (3)$$

In this case, the LTP intra-beam interference has led to a significantly broadened and irregular diffracted beam intensity profile recorded with the LTP-II CCD detector (Fig. 1a). The profile shape has strong variation along the grating clear aperture leading to unacceptably high error of the recorded diffraction angle (Fig. 1b).
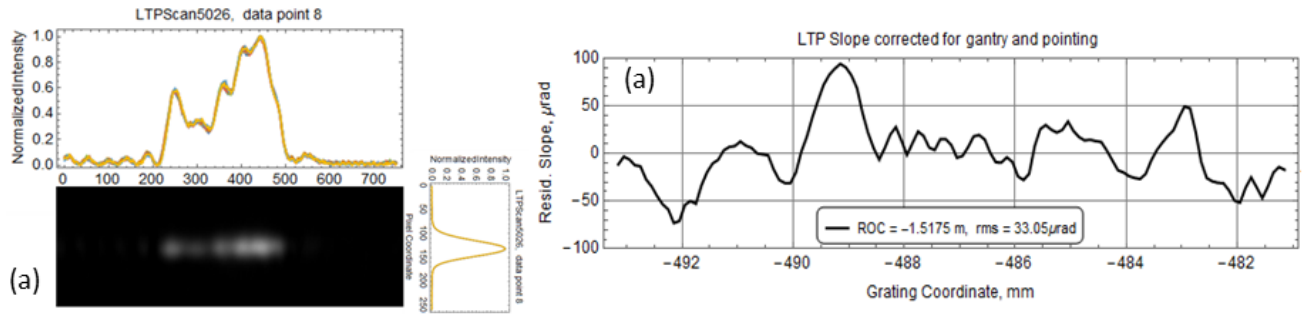
Figure 1. (a) The diffracted light beam intensity distribution recorded with the LTP-II CCD detector in groove density measurements with the ALS AMBER beamline VLS grating placed in the first order Littrow configuration. The grating is specified by the polynomial parameters in Eq. (3). (b) The diffraction angle variation measured over a ~12 mm long tangential trace; the best-fit linear trend characterized with an equivalent radius of curvature of ~ 1.5 m is detrended. Note that the single 12-mm trace corresponds to the entire angular dynamic range of the LTP measurements, whereas the total length of the grating clear aperture is 80 mm.

Moreover, when measuring the AMBER VLS grating, the LTP-II can perform a single measuring scan only over a 12-mm region out of the total length of the grating clear aperture of 80 mm. Therefore, to thoroughly characterize the grating, one needs to stitch together at least 8 scans (assuming 2 mm overlap), performed with different pitch tilts of the grating. Such stitching requires high-precision absolute measurements of the incidence and diffraction angles for each point of a scan, which is extremely difficult because of the uncertainty in the absolute referencing of the LTP-II angular coordinate system.

2.2 Optical microscope measurements with x-ray VLS diffraction grating

Recently, the application of interferometric microscopes capable of direct measurements of the two dimensional (2D) grating surface topography with significantly higher spatial resolution than possible with an LTP has been suggested and brought to everyday practice at x-ray facilities [7].

Figure 2a shows the surface height distribution measured with the ALS XROL interferometric microscope near the center of the same AMBER grating as in Fig. 1. The microscope is equipped with 50× objective and 1× zoom lens. In the grating metrology with the microscope, the spatial frequency of the peak in the averaged 1D PSD in the horizontal direction (Fig. 2b) is used as a measure of the area's groove density.

Multiple measurements along the grating clear aperture provide the groove density distribution shown in Fig. 3a. The distribution is fitted with the specified polynomial function (1) to extract the parameters of the VLS grating.
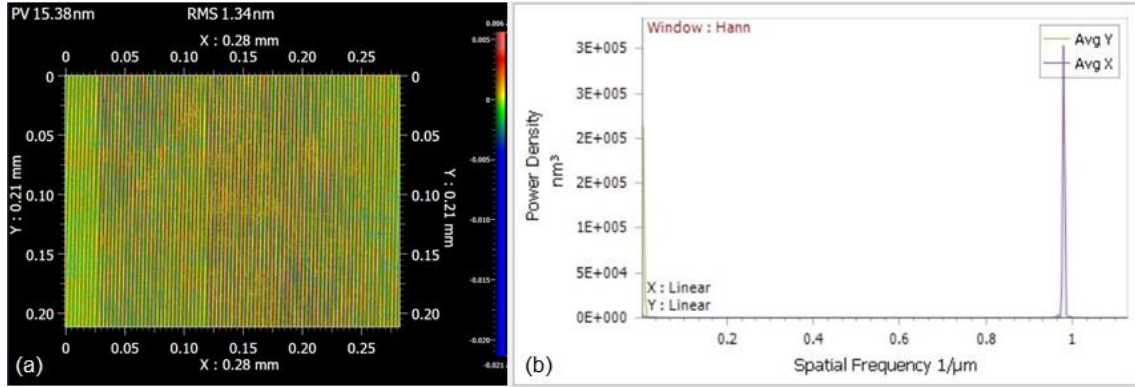
Figure 2. (a) A local height distribution measured using the interferometric microscope over the center area of the same AMBER VLS grating as in Fig. 1. (b) The 1D PSD_X distribution corresponding to the grating height topography in plot (a). The microscope is equipped with 50× objective and 1× zoom lens.

The solid line in Fig. 3a shows the best-fit third-order polynomial with the values of the parameters and their fit errors presented in Table 1. The precision of the VLS grating metrology achieved in this measurement is characterized by the residual groove density variation in Fig. 3b via the root-mean-square (rms) variation of the point that is about 0.4 line/mm or, equivalently for this 1000 lines/mm grating, 0.4 µm/mm.
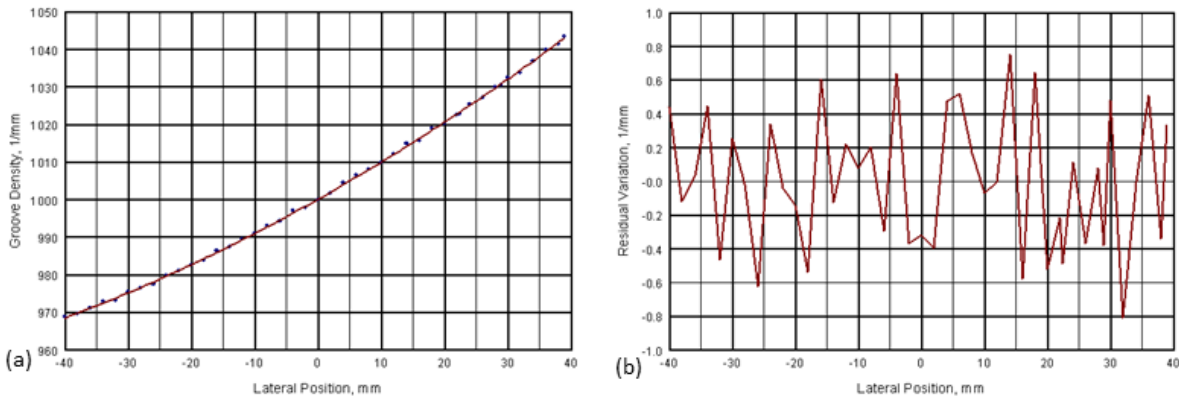
Figure 3. (a) The groove density distribution (dots), as measured using the interferometric microscope over the 80-mm clear aperture of the same AMBER VLS grating as in Fig. 1. The best-fit third-order polynomial function is shown with the solid red line. The best-fit values of the polynomial parameters and their fit errors (standard deviations) are presented in Table 1. (b) Residual (after subtraction of the best-fit third-order polynomial function) groove density variation. The precision of the groove density metrology achieved in this measurement is characterized by the value of the standard deviation for the points in plot (b) that is about 0.4 line/mm or, equivalently for this 1000 lines/mm grating, 0.4 µm/mm.

Table 1: The polynomial parameters of the groove density distribution of the AMBER VLS grating as specified and measured with the XROL interferometric microscope.

Parameter	Specified	Measured	Measurement error
g_0, lines/mm	1000.1	1000.097	0.096
g_1, lines/mm^2	0.95381	0.949654	0.0066
g_2, lines/mm^3	0.004007	0.0039305	0.00013
g_3, lines/mm^4	-3.304×10^{-6}	-1.154×10^{-6}	6.2×10^{-6}

Comparison of the results of the LTP-II (Fig. 1) and interferometric microscope (Fig. 3) measurements suggest a significantly higher precision of the later technique. However, the measurement precision appears to be inadequate for

the required 20% accuracy on the parameter g_3. An improvement by an order of magnitude is required for interferometric microscope measurements with the VLS x-ray gratings such as the one developed the ALS AMBER beamline.

Moreover, the accuracy of the interferometric measurements can be significantly different from the achieved precision. There are notable sources of systematic errors, such as geometrical distortion and dependence of the detector effective pixel size on the microscope objective/zoom lens arrangement (see Sec. 4 below).

Our project, the first results of which we discuss in this paper, aims to overcome the limitations of the existing interference microscopy metrology with VLS x-ray gratings. To resolve the systematic error problem, we develop and apply different techniques for precision calibration of the microscope, followed by high-accuracy data restoration based on the calibration. To improve the accuracy of the metrology we develop and implement sophisticated data acquisition and analysis methods and procedures. However, a detailed discussion of the later part of the project is out of the scope of the present publication.

3. MICROSCOPE'S GEOMETRICAL DISTORTION AND ITF CALIBRATION

In this section, we discuss the effects of the geometrical distortions in the interferometric microscope measurements with topographical objects (surfaces under test, SUTs) like the diffraction gratings. Although the distortion has a negligible effect on the surface roughness measurements, it can cause a significant misrepresentation of the SUT topography in both height and special frequency (PSD) domains (see, for example, Refs. [18-25] and references therein).

Figure 4 illustrates the most common geometrical radial distortions of an image of a straight-line grid test sample. Both the negative radial ("pincushion" type) distortion (Fig. 4a) and positive radial ("barrel" type) distortion (Fig. 4c), if present in a microscope measurement, result in a nonlinear magnification in the grating topography from the center to the periphery of the measured area. Therefore, precision calibration and, if necessary, correction of the interferometric microscope measurements for geometrical distortion is vital for high-accuracy metrology.
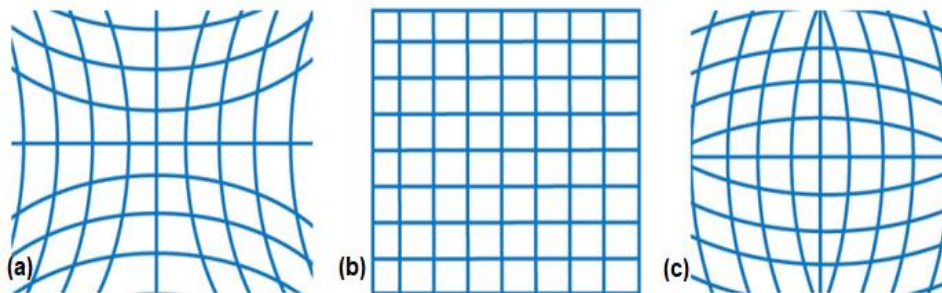
Figure 4. Illustration of the geometrical radial distortion of an image of a straight-line grid test sample: (a) negative radial ("pincushion" type) distortion, (b) no distortion, and (c) positive radial ("barrel" type) distortion.

In this section, we describe test standards (Sec. 3.1) and data acquisition and analysis procedures (Secs. 3.2 and 3.3) developed and used for characterization of interferometric microscopes and demonstrate the efficiency of the calibration techniques in measurements with the ALS XROL interferometric microscope.

3.1 Test standards for characterization of interferometric microscopes

To characterize the microscope's systematic errors, geometrical distortion, and ITF over an increased effective dynamic range, we use specially designed test standards and artifacts (see, for example, Refs. [26-33] and references therein). For the ITF calibration of optical microscopes, binary pseudo-random array standards patterned with the uniformly redundant [9,10] and highly randomized binary [29] arrays (URA BPRAs and HR BPRAs) with fundamental (smallest) feature size of 30 – 2,500 nm are now available [30,31].

By design, the URA and HR BPRA patterns have inherent PSD distributions that are perfectly constant when evaluated over the entire array. In application to the ITF characterization of a surface profilometers, the deviation of the measured PSD can be used as a measure of the tool's ITF.

Because of a relatively well-ordered layout of the URA-based BPRA patterns, these standards, besides their use for ITF calibration, can be used for characterization of the microscope geometrical distortion. In this work (see Sec. 3.3, below), we use the A1 and B1 URA PBRA patterns with the elementary sizes of 2.5 µm and 1.2 µm of a 2-in diameter BPRA standard described in detail in Refs. [31,32] – Fig. 5. The etched depth of the patterns is about 95 nm as seen on the corresponding sections along the slice line depicted in the 2D images.
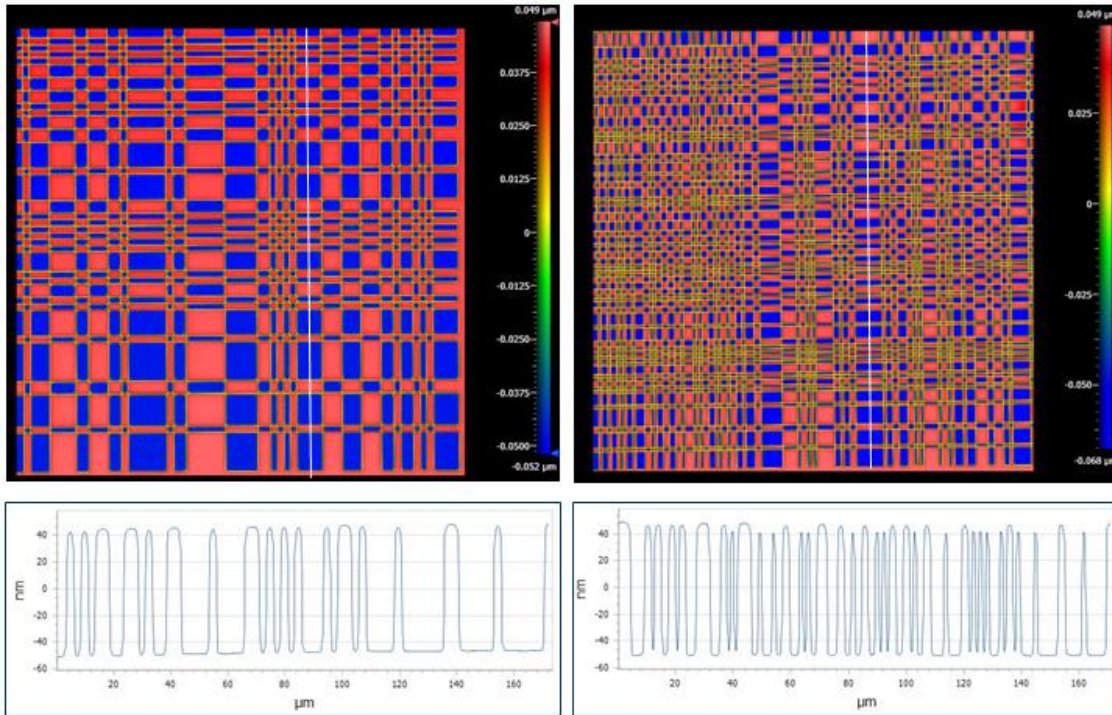
Figure 5. The A1 (left) and B1 (right) URA PBRA patterns with the elementary sizes of 2.5 µm and 1.2 µm as measured with the ALS XROL interferometric microscope equipped with 50× objective at 1× zoom. The etched depth of the patterns is about 95 nm as seen on the corresponding sections along the slice line depicted in the 2D images. The 2-in diameter BPRA standard containing the shown patterns is described in detail in Refs. [31,32].

The 2-in diameter BPRA standard containing the patterns depicted in Fig. 5 has 8 BPRA patterns etched to the substrate. The BPRA patterns A1, B1, C1 and D1 with the smallest fundamental (elementary) sizes of 2.5 µm, 1.2 µm, 800 nm, and 400 nm, respectively, are patterned with a uniformly redundant array (URA) [9,10]; whereas, the patterns A2, B2, C2 and D2 with the elementary sizes of 2.501 µm, 1.201 µm, 801 nm, and 401 nm are designed according to the highly randomized (HR) BPR arrays described in Ref. [29]. The step-function pattern E1 that is also etched to the standard is used for cross-comparison investigations when modeling of the ITF of the microscope (see the corresponding discussion in Ref. [34]). To calibrate the ITF of a microscope in higher resolution configuration, we use a high-resolution HR BPRA standard fabricated on a 1-in diameter super-polished silicon substrate [31,32]. This standard has three HR BPRA patterns with the elementary sizes of 241 nm, 161 nm, and 81 nm, respectively.

The HR BPRAs have been specially designed to eliminate the limitation of the URA-based BPRA patterns related to a relatively well-ordered layout that results in an increased noise in the PSD distributions measured over cropped areas of the URA BPRA patterns [29]. Consequently, the ITF measurements discussed in this paper (Sec. 3.4) are performed over the HR BPRA patterns.

For increased accuracy of the geometrical distortion calibration, we have also designed and fabricated traditional checkerboard test artifacts (Fig. 6) [30,31] using the nano-fabrication capabilities at the LBNL Molecular Foundry (MF). The checkerboard sample has two patterns with the elementary sizes 3.0 µm and 1.5 µm etched to the depth of about 15 nm on 1-in diameter super-polished silicon substrate.
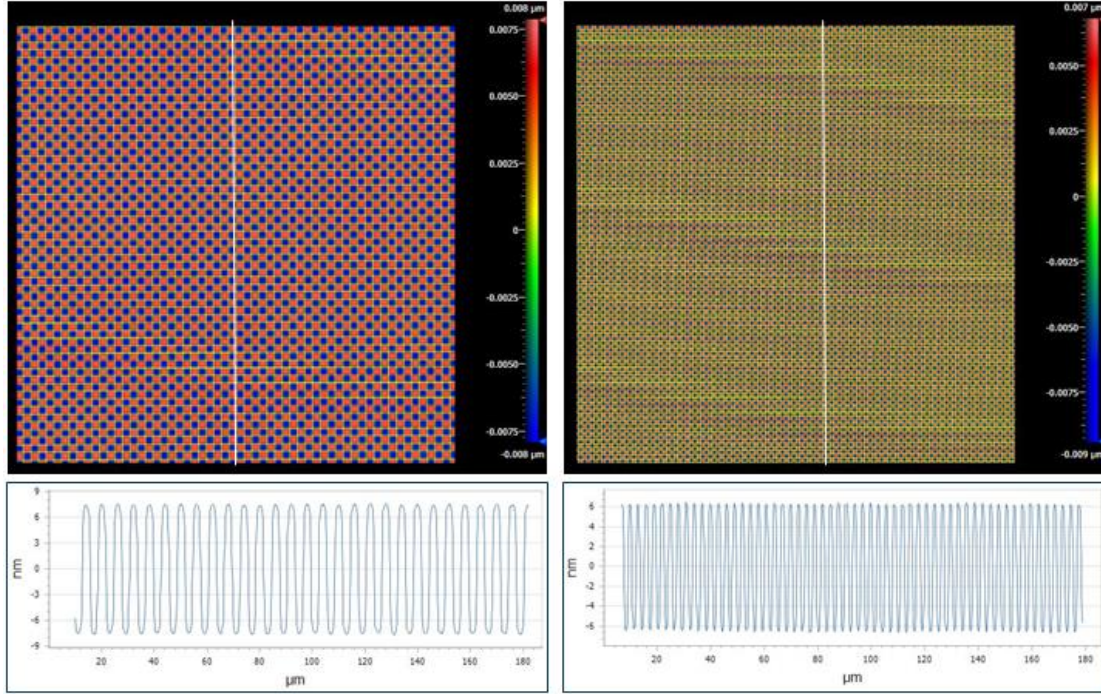
Figure 6. The A1 (left) and B1 (right) URA PBRA patterns with the elementary sizes of 3.0 µm and 1.5 µm as measured with the ALS XROL interferometric microscope equipped with 50× objective at 1× zoom. The etched depth of the patterns is about 15 nm as seen on the corresponding sections along the slice line depicted in the 2D images. The 2-in diameter BPRA standard is described in detail in Refs. [31,32].

3.2 Characterization of the microscope geometrical distortion

For the measurements discussed in this paper, the data acquisition and preliminary data processing is performed with the microscope software. The preprocessing includes subtraction of the reference topography, measured and averaged over a number of unpatterned areas of the standard, and detrending of the best-fit plane surface. No filtering is applied.

For the geometric distortion calibration, both URA BPRA and checkerboard samples were used. The calibration data processing consists in locating and matching characteristic features of the measured and designed (ideal) test patterns (Fig. 7).
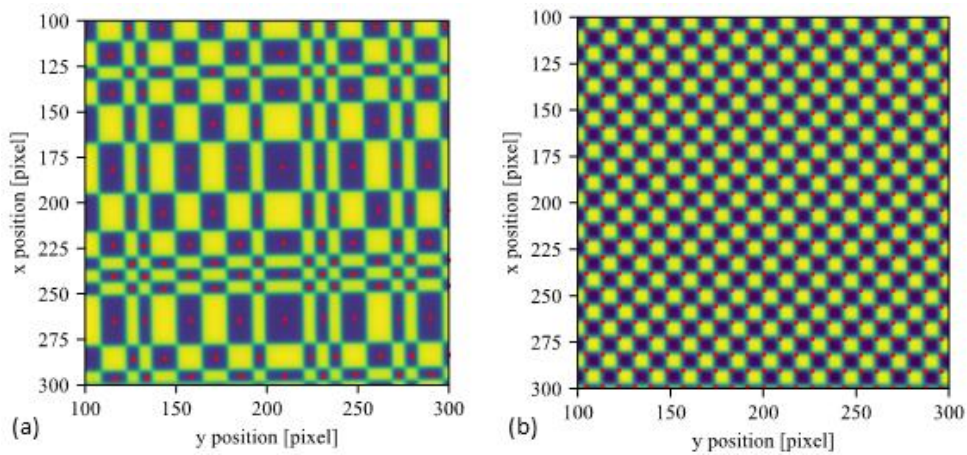
Figure 7. (a) A 200 x 200-pixel section of a 1000 x 1000-pixel image of the 1.2 µm URA BPRA pattern; red dots indicate rectangle centers found by the developed feature-finding algorithm. (b) A 200 x 200-pixel section of a 1000 x 1000-pixel image of the 1.5 µm checkerboard; red dots indicate corners found by the algorithm [36] described in the text.

In the case of the URA BPRA data, the positions of the rectangle centers are found using ad hoc code developed for this purpose. For the traditional checkerboard samples, there are existing implementations of sophisticated algorithms, available, for example, in the Open-Source Computer Vision (OpenCV) library [35], for locating the checkerboard corners with high accuracy.

Here, for finding the corners of the checkerboard elements (Fig. 7b), we use a method described in Ref. [36] and implemented in OpenCV, which is based on a localized Radon transform implemented by box filters and provides high subpixel accuracy. The checkerboard calibration results acquired with the method [36] are less noisy compared to those obtained with the URA BPRA data. Therefore, although the results from the two types of samples are consistent, the calibration results from the checkerboard data will be presented here.

The checkerboard image processing is performed in Python using camera calibration routines from the OpenCV library. First, the found corners of the recorded checkerboard image (Fig. 7b) are identified with the projection of the corners of an ideal checkerboard sample from 3D space onto the camera image plane using the pinhole camera model (see, for example, Ref. [37]). Next, the position, rotation, tilt, and magnification of the ideal sample (extrinsic parameters) are varied and the best fit to the measured corners is found. The fitting model also includes lens distortion, in the form of the lowest-order radial distortion term with the distortion coefficient k_1. The distortion procedure shifts each point (x, y) in the image plane by an amount depending on its displacement $(d_x = x - c_x, d_y = x - c_y)$ from a principal (aka the central) point (c_x, c_y), so that

$$x' = d_x(1 + k_1 r^2) + c_x, \tag{3a}$$

$$y' = d_y(1 + k_1 r^2) + c_y, \tag{3b}$$

where $r^2 = d_x^2 + d_y^2$.

Figure 8 shows the residual distances between the measured checkerboard corners from the image (Fig. 7a) and the best-fit projection of the ideal checkerboard corners. When the distortion effect is omitted from the projection model (Fig. 8a), the displacement exhibits r^3 dependence with residual distance of up to two pixels at the image corners. Accounting in the projection model for the lowest-order radial camera distortion, given by Eq. (3), the measured and ideal checkerboard patterns match well (Fig. 8b).
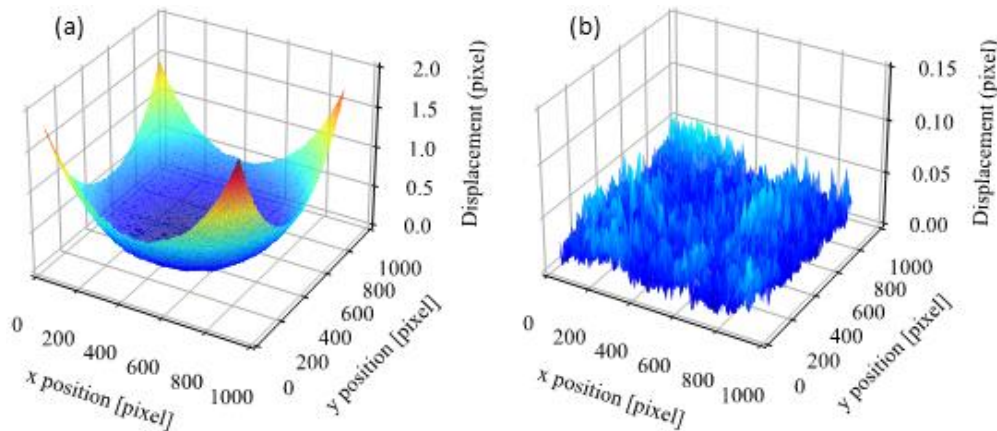
Figure 8. Displacement (in pixels) between the checkerboard corners found from the image and those of an ideal checkerboard projected onto the image, rotating and translating for the best fit. (a) Projection neglects camera distortion; (b) projection accounts for lowest-order radial camera distortion. Note the change in vertical scale.

Thus, the observed lens distortion is well described by the lowest-order term described above, with the residual distance between projected and measured corners less than 0.05 of a pixel. For the data in Fig. 8, the best-fit distortion parameter is 6.819(7)×10⁻⁹ pixel⁻² and the principal point is (473 px, 515 px). Using the checkerboard square size of 1.5 µm as a

reference (due to the high accuracy of the USED nano-fabrication process), the performed fitting also allows us to measure the corrected microscope's pixel size to be 0.17289(1) µm.

Analyzing measurements of different areas of the checkerboard sample allowed us to confirm that the observed distortion is due to the microscope and is not intrinsic to the sample. (It also revealed a fabrication defect in the sample, appearing as a "seam" where stitched regions of the pattern were mis-registered by ~40 nm.)

The extracted geometrical distortion calibration parameters can be used to reconstruct the surface topography of a measured sample by applying the inverse coordinate transformation and resampling using bilinear interpolation. The results of this procedure applied to measurements of a uniform grating are discussed in Sec. 4.1.

3.3 The microscope ITF calibration

For our ITF calibration of metrology profilometers, the preprocessed height distribution data taken over a suitable BPRA standard pattern is processed with custom software developed for PSD processing of the data, ITF model parametrization, and ITF-based deconvolution of the measured data [30-32,34]. Figure 9 presents the software screenshot corresponding to processing a measurement over the 1-in Dia. HR BPRA pattern with the elementary size of 81 nm performed with the interferometric microscope equipped with the 50× objective and 1× zoom lens.
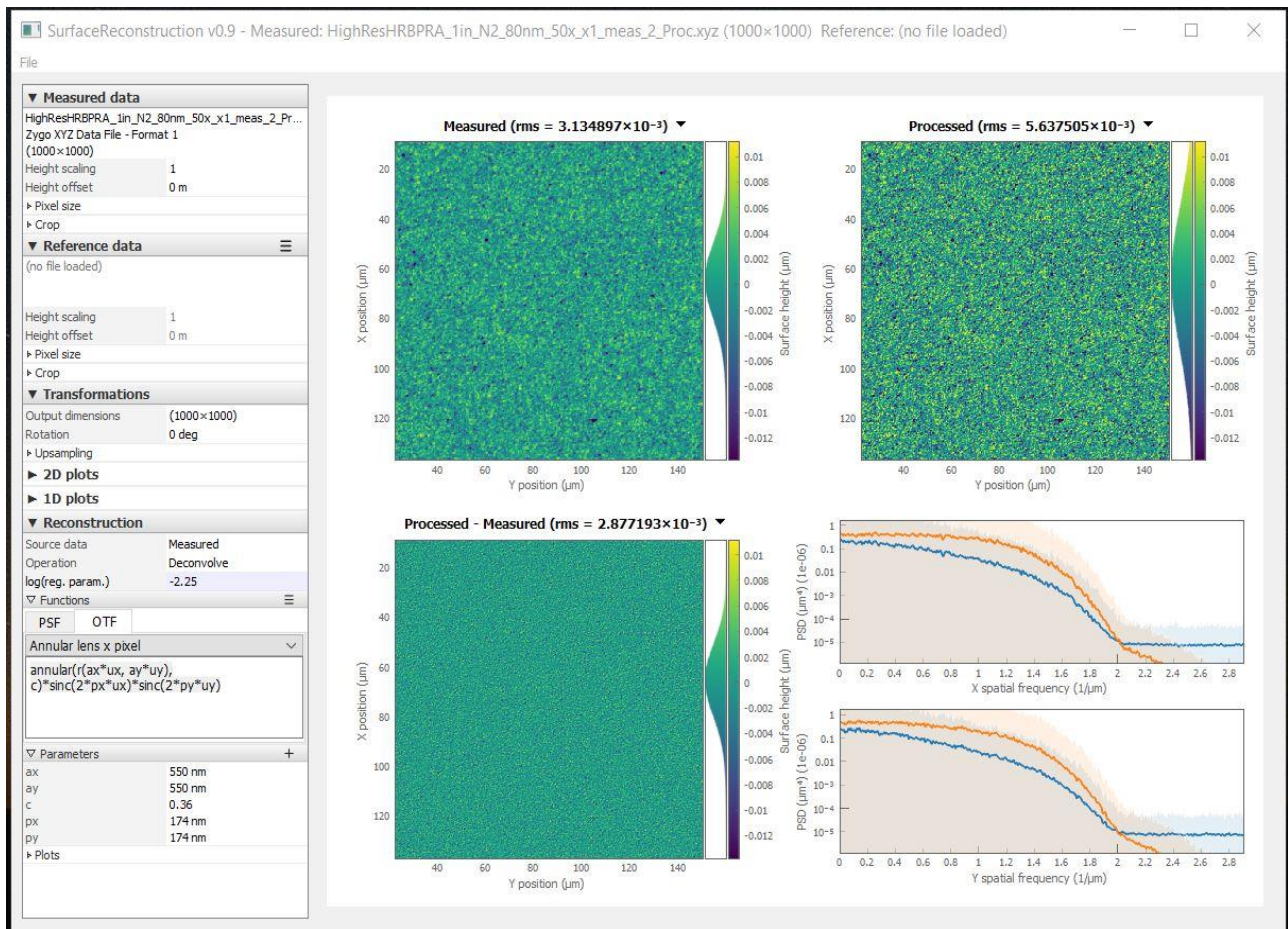
Figure 9. A screenshot of the original software developed for the ITF calibration of metrology profilometers and ITF-based deconvolution of the measured data. The data shown has been recorded with the HR BPRA pattern with the elementary size of 81 nm using the ALS XROL interferometric microscope equipped with the 50× objective and 1× zoom lens. The 1D PSD distributions of the measured (blue lines) and deconvolved (orange lines) are shown in the bottom right part of the screenshot. Deconvolution is performed with a simplified linear model that considers only the transfer functions of the lens and detector pixels [34,38] (see the discussion in the text).

In this case depicted in Fig. 9, the spatial resolution is significantly lower than if it were limited by the effective pixel size of about 172 nm. The observed resolution corresponds to the Abbe limit of 500 nm for the light wavelength of 550 nm and objective numerical aperture (NA) of 0.55.

The software depicted in Fig. 9 is capable of deconvolution of the measured data using the measured and parametrized ITF of the tool in use. The problem of derivation of a high-confidence analytical model of the microscope in different measurement arrangement is rather nontrivial problem [34,38-43] and is out of the scope of the present work. Nevertheless, some interesting results are obtained even with a simplified linear model that considers only the transfer functions of the lens and detector pixels [34,38] (see Sec. 3.4).

The immediate result of the deconvolution depicted in Fig. 9 is the increased (by a factor of ~ 1.8) roughness of the deconvolved topography compared to that of the measured data. From the point of view of the measurements with VLS x-ray gratings, the more important result is that the deconvolution allows recovering the PSD spectrum at spatial frequencies above ~1.2 μm^{-1} by a factor of ~10 and even more at higher frequencies. We can also conclude that the upper limit of the groove density range available in measurements with an interferometric microscope is ~1,800 lines/mm. Our goal is to demonstrate and even extend the range with a more sophisticated data acquisition and processing techniques under development in the scope our DOE STTR/SBIR projects.

4. EFFECT OF MICROSCOPE LENS DISTORTION ON GRATING METROLOGY

In metrology of VLS x-ray gratings, the lens distortion of the ALS XROL interferometric microscope observed and calibrated with the checkerboard test sample (Sec. 3.2) shifts the apparent grating spatial frequency by different amounts depending on the position in the recorded grating topography. To understand the scale of the corresponding error in the measured grating groove density (grating spatial frequency), we use an optical blazed grating with uniform 600 lines/mm groove density in a clear aperture of about 50 mm × 50 mm. A series of three measurements of different areas of the grating (grating center and two areas shifted by ±10 mm) was performed with the interferometric microscope arrangement (50× objective and 1× zoom) calibrated with the checkerboard as described in Sec. 3.2. The measurements are sufficient for separation of the effects of the microscope lens distortion and the grating imperfection.

Figure 10 shows the apparent grating frequency as a function of location in each of the three measurements. The local grating frequency is evaluated over subareas of width 50 pixels using a windowed Fourier transform peak finder with window size 200 pixels and step size 50 pixels.
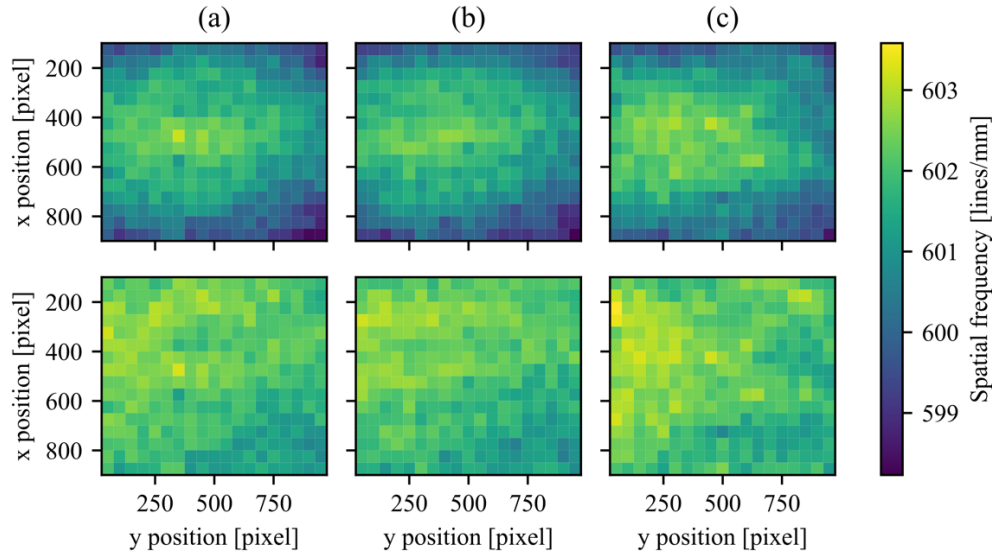
Figure 10. Position dependence of the apparent grating frequency for images of three different areas of the uniform grating sample shifted by ±10 mm extracted from the uncorrected surface height distribution data (top row) and (bottom row) from the same data corrected using the geometrical distortion calibration in Sec. 3.2. Scaled value of frequency is found using the pixel size extracted from the distortion calibration.

The top row in Fig. 10 shows the grating frequency variation extracted from the raw data, uncorrected for the microscope lens distortion. The apparent frequency is higher at the center of each measurement than at the edges, a characteristic result of radial distortion. The bottom row shows the grating frequency variation with the same data as in the top row but corrected using the geometrical distortion calibration discussed in Sec. 3.2.

With the calibration, the radial variation of the apparent grating frequency has been removed, and the range of observed frequencies has been compressed. This is also apparent in the corresponding grating frequency histograms presented in Figure 11.
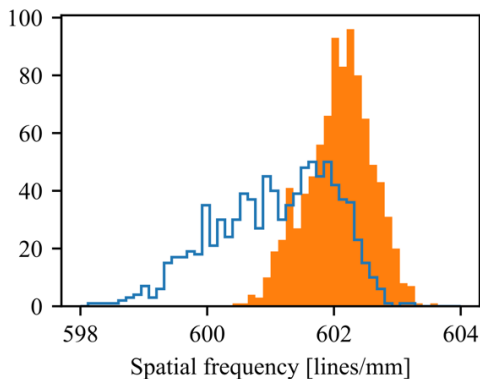
Figure 11. Histograms of the grating frequency variations extracted (blue, unfilled) from the uncorrected data depicted in the top row of Fig. 10 and (orange, filled) from the corrected data depicted in the bottom row of Fig. 10.

Note that there is a residual trend in the position dependence of the apparent frequency of the corrected data (the bottom row in Fig. 10) with higher frequencies at the upper left of each image. This may be due to the residual effect of sample tilt, which will be addressed in future work.

5. DISCUSSION AND CONCLUSIONS

We have discussed progress in work towards precision measurements of variable-line-spacing x-ray diffraction grating surface topology using interferometric microscopes. The technique is based on optical microscope measurements of the PSDs of grating surface sub-areas and estimation of the groove density values from the spatial frequency of the corresponding PSD peaks.

We have shown that this technique is capable of reliable characterization of VLS gratings with rapid groove density variation, for which traditional methods such as long trace profilometry fail. However, the currently available accuracy of optical microscope measurements, on the level of ~ 0.4 µm/mm, is not enough for high-confidence determination of higher order polynomial parameters g_2 and g_3 specified for the grating groove density variation. We need to improve the accuracy by a factor of 5-10.

To advance the technique with higher accuracy and dynamic range of groove density variation than is currently available and make it suitable for integration into VLS x-ray grating fabrication processes, we are developing instrument characterization and data processing methods: image reconstruction to correct for distortion and blurring by the interferometric microscope, multi-image super-resolution data acquisition to increase resolution beyond the single-image limit, and high accuracy image stitching to increase the measurement area. In this first publication on the project, we have concentrated on precision calibration and correction of the interferometric microscope measurements for lens distortion and have tested a procedure for high accuracy measurement of the effective image pixel distribution.

Using checkerboard and URA BPRA test artifacts, we have experimentally demonstrated significant distortion of the imaged artifact pattern due to microscope lens distortion. We have extracted a precision parametrized model of the distortion, allowing us to remove it in reconstructed data.

As a demonstration, the resulting calibration was used to remove geometrical distortion from the measurement of a uniform grating sample, increasing the precision and accuracy of the grating frequency measurement.

We have also given results of measurements of the microscope instrument transfer function, which indicate that groove densities of up to 1800 lines/mm can be characterized with the interferometric microscope. The results of the ITF calibration can be used to improve the measurement resolution.

ACKNOWLEDGEMENTS

DISCLAIMER

REFERENCES

[1] Follath, R., and Senf, F., "New plane-grating monochromators for third generation synchrotron radiation light sources," Nucl. Instrum. and Meth.A390, 388-394 (1997); doi: 10.1016/S0168-9002(97)00401-4.

[2] Howells, M. R., "Gratings and monochromators in the VUV and soft x-ray spectral region," in: [Handbook of Optics], M. Bass, Ed., 3rd Ed., McGraw-Hill, New York, 2001, Vol. 5, Ch. 38.

[3] Idir, M. and Yashchuk, V. V., "Optical and X-ray metrology," in: D. Mills, H. Padmore (Eds.), [X-Ray Opt. BES Light Source Facilities], U.S. Department of Energy, Office of Science, Potomac, MD, 2013; https://science.osti.gov/-/media/bes/pdf/reports/files/X-ray_Optics_for_BES_Light_Source_Facilities_rpt.pdf.

[4] Irick, S. C. and McKinney, W. R., "Measurement of diffraction gratings with a long trace profiler with application for synchrotron beamline gratings," AIP Conf. Proc. 417, 118-121 (1997). ; https://doi.org/10.1063/1.54581.

[5] Cocco, D., Sostero, G., Zangrando, M., "Technique for measuring the groove density of diffraction gratings using the long trace profiler," Rev. Sci. Instrum. 74 (2003) 3544–3548; https://doi.org/10.1063/1.1584080.

[6] I. Lacey and V. V. Yashchuk, "Characterization of Groove Density Variation of VLS gratings with ALS XROL LTP–II in different operation modes," Proc. SPIE 11492, 114920D/1-16 (2020); doi: 10.1117/12.2568705.

[7] Yashchuk, V. V., McKinney, W. R., Artemiev, N. A., "Ex situ metrology of x-ray diffraction gratings," Nucl. Instrum. Meth. A710, 59–66 (2013); https://doi.org/10.1016/j.nima.2012.10.109.

[8] Yashchuk, V. V., Artemiev, N. A., Lacey, I., McKinney, W. R., and Padmore, H. A., "Advanced environmental control as a key component in the development of ultra-high accuracy ex situ metrology for x-ray optics," Opt. Eng. 54(10), 104104 (2015); doi: 10.1117/1.OE.54.10.104104.

[9] Fenimore, E. E., and Cannon, T. M., "Coded aperture imaging with uniformly redundant arrays," Appl. Opt. 17(3), 337–347 (1978); doi: ttps://doi.org/10.1364/AO.17.000337.

[10] Caroli, E., Stephen, J. B., Cocco, G. Di., Natalucci, L., and Spizzichino, A., "Coded aperture imaging in x- and gamma-ray astronomy," Space Sci. Rev. 45, 349–403 (1987); doi: https://doi.org/10.1007/BF00171998.

[11] Warwick T., and Reininger R. "Redesign of MAESTRO beam line with a Variable Included Angle Varied Line Space Grating (VIA VLS) monochromator," ALS Light Source Note LSBL-982RevA, January (2010).

[12] Jakstas, A., Kausinis, S., and Flugge, J., "Investigation of Calibration Facilities of Precision Line Scales," ISSN 1392 – 1207. Mechanika. 3(53), 62-67 (2005); doi: 10.5755/J01.MECH.53.3.13034 Corpus ID: 73596533.

[13] Cocco, D., and Thomasset, M., "Measurement of groove density of diffraction gratings," in: [Modern Developments in X-Ray and Neutron Optics], Springer-Verlag, 2008, pp. 207–211, ISBN: 978-3-540-74560-0.

[14] F. Siewert, H. Lammert, G. Reichardt, U. Hahn, R. Treusch, R. Reininger, Inspection of a Spherical Triple VLS-Grating for Self-Seeding of FLASH at DESY, AIP Conf. Proc. 879 (2007) 667–670. https://doi.org/10.1063/1.2436150.

[15] Thomasset, M., Dvorak, J., Brochet, S., Dennetiere, D., and Polack, F., "Grating metrology for X-ray and V-UV synchrotron beamlines at SOLEIL," Rev. Sci. Instrum. 90, 021714 (2019); https://doi.org/10.1063/1.5055284.

[16] Yashchuk, V. V., Lacey, I., Anderson, K., Dickert, J., Smith, B.V., and Takacs, P. Z., "Multifunctional light beam source for surface slope measuring long trace profilers," Proc. SPIE 11492, 1149205/1-18 (2020); doi: 10.1117/12.2570462.

[17] The ALS AMBER beamline, https://www.facebook.com/ALS-Beamline-601-AMBER-100982529986098/.

[18] Devernay, F., and Faugeras, O. D., "Automatic calibration and removal of distortion from scenes of structured environments," in: Investig. Trial Image Process., SPIE, 1995: pp. 62–72; https://doi.org/10.1117/12.218487.

[19] Fitzgibbon, A. W., "Simultaneous linear estimation of multiple view geometry and lens distortion," in: Proc. 2001 IEEE Comput. Soc. Conf. Comput. Vis. Pattern Recognit. CVPR 2001, IEEE Comput. Soc, Kauai, HI, USA, 2001: p. I-125-I–132. https://doi.org/10.1Kikuta109/CVPR.2001.990465.

[20] Yoneyama, S., Kikuta, H., Kitagawa, A., and Kitamura, K., "Lens distortion correction for digital image, correlation by measuring rigid body displacement" Opt. Eng. 45(2), 023602 (2006); https://doi.org/10.1117/1.2168411.

[21] Zang, D., Luo, M., and Alrola, D. D., "Displacement/strain measurements using an optical microscope and digital image correlation," Opt. Eng. 45(3), 033605/1-9 (2006); https://doi.org/10.1117/1.2182108.

[22] Pan, B., Yu, L., Wu, D., and Tang, L., "Systematic errors in two-dimensional digital image correlation due to lens distortion," Opt. Las. Eng. 51, 140–147 (2013); http://dx.doi.org/10.1016/j.optlaseng.2012.08.012.

[23] Ekberg, P., Su, R., and Leach, R., "High-precision lateral distortion measurement and correction in coherence scanning interferometry using an arbitrary surface," Opt. Exp. 25(16), 18703-18712 (2017); https://doi.org/10.1364/OE.25.018703.

[24] Qian, W., Li, J., Zhu, J., Hao, W., and Chen, L., "Distortion correction of a microscopy lens system for deformation measurements based on speckle pattern and grating," Opt. Las. Eng. 124, 105804/1-9 (2020); https://doi.org/10.1016/j.optlaseng.2019.105804.

[25] Wu, D, Qian, L, and Zhu, P., "The distortion elimination of an optical microscope based on optimized windowed Fourier transform," Precision Eng. 70, 124–134 (2021); https://doi.org/10.1016/j.precisioneng.2021.02.003.

[26] Yashchuk, V. V., McKinney, W. R., and Takacs, P. Z., "Test surfaces useful for calibration of surface profilometers," United States Patent No.: 8,616,044.

[27] Yashchuk, V. V., McKinney, W. R., and Takacs, P. Z., "Binary pseudorandom grating standard for calibration of surface profilometers," Opt. Eng. 47(7), 073602-1-5 (2008); https://doi.org/10.1117/1.2955798.

[28] Barber, S. K., Anderson, E. D., Cambie, R., McKinney, W. R., Takacs, P. Z., Stover, J. C., Voronov, D. L., and Yashchuk, V. V., "Binary pseudo-random gratings and arrays for calibration of modulation transfer function of surface profilometers," Nucl. Instr. and Meth. A 616, 172-182 (2010); https://doi.org/10.1016/j.nima.2009.11.046.

[29] Yashchuk, V. V., Babin, S., Cabrini, S., Chao, W., Griesmann, U., Lacey, I., Marchesini, S., Munechika, K., Pina-Hernandez, C., and Roginsky, A., "Binary pseudo-random array test standard optimized for characterization of large field-of-view optical interferometers," Proc. SPIE 11490, 114900W/1-8 (2020); doi: 10.1117/12.2568309.

[30] Munechika, K., Cabrini, S., Chao, W., Lacey, I., Pina-Hernandez, C., Rochester, S., and Yashchuk, V. V., "Binary pseudo-random array test standard optimized for characterization of interferometric microscopes," Proc. SPIE 11817, 1181704/1-10 (2021); doi: https://doi.org/10.1117/12.2594995.

[31] Munechika, K., Rochester, S., Chao, W., Lacey, I., Pina-Hernandez, C., and Yashchuk, V. V., "Binary pseudo-random array standards for calibration of 3D optical surface profilers used for metrology with aspheric x-ray optics," SPIE Optics and Photonics 2022, Conference OP323: Interferometry XXI, Paper No.: OP323-16; Tracking No.: OP22O-OP323-16 (San Diego, August 21-25, 2022); this conference.

[32] Yashchuk, V. V., Munechika, K., Rochester S., Chao, W., Lacey, I., Pina-Hernandez, C., and Takacs, P. Z., "Reliability investigation of the instrument transfer function calibration technique based on binary pseudo-random array standards", in SPIE Optics and Photonics 2022, Conference OP220: Advances in Metrology for X-Ray and EUV Optics X, (San Diego, August 21-25, 2022); this conference.

[33] Griesmann, U., Munechika, K., Renegara, T. B., Zheng, X. A., Soons, J. A., Chao, W., Lacey, I., Pina-Hernandez, C., Takacs, P. Z., and Yashchuk, V. V., "Characterization of surface texture-measuring optical microscopes using a binary pseudo-random array standard," SPIE Optics and Photonics 2022, Conference OP323: Interferometry XXI, Paper No.: OP323-21; Tracking No.: OP22O-OP323-21 (San Diego, August 21-25, 2022); this conference.

[34] Takacs, P. Z., Rochester, S., Lacey, I., Munechika, K., and Yashchuk, V. V., "Calibration, modeling, parameterization, and verification of the Instrument Transfer Function of an interferometric microscope," SPIE Optics and Photonics 2022, Conference OP323: Interferometry XXI, Paper No.: OP323-13; Tracking No.: OP22O-OP323-13 (San Diego, August 21-25, 2022); this conference.

[35] Bradski, G.R and Kaeller, A., [Learning OpenCV- Computer Vision with the OpenCV], 1st Ed., O'Reily Media, Inc., Sebastopol (2008).

[36] Duda, A. and Frese, U., "Accurate Detection and Localization of Checkerboard Corners for Calibration," in: [29th British Machine Vision Conference (BMVC-29)], BMVA Press, Newcastle, 2018; http://bmvc2018.org/contents/papers/0508.pdf.

[37] Hartley, R. and Zisserman, A., [Multiple View Geometry in Computer Vision], Cambridge University Press, New York, 2003.

[38] Church, E. L., Vorburger, T. V., and Wyant, J. C., "Direct comparison of mechanical and optical measurements of the finish of precision machined and optical surfaces," Opt. Eng., 24(3), 388-395 (1985); https://doi.org/10.1117/12.944964.

[39] Boreman, G. D., [Modulation Transfer Function in Optical and Electro-optical Systems], SPIE Press, Bellingham, Washington (2001).

[40] ISO, 25178-600: Geometrical Product Specification (GPS) – Surface Texture: Areal – Part 600: Metrological Characteristics for Areal-topography Measuring Methods (International Organization for Standardization, 2019); https://www.iso.org/standard/67651.html.

[41] de Villiers, G. and Pike, E. R., [The Limits of Resolution], CRC Press, London & New York (2019).

[42] Foreman, M. R., Giusca, C. L., Coupland, J. M., Torok, P., Leach, R. K., "Determination of the transfer function for optical surface topography measuring instruments - a review," Meas. Sci. Technol. 24, 052001/1-18 (2013); doi:10.1088/0957-0233/24/5/052001.

[43] de Groot, P. J., "The instrument transfer function for optical measurements of surface topography," J. Phys. Photonics 3, 024004/1-16 (2021); doi: https://doi.org/10.1088/2515-7647/abe3da.